Contents lists available at SciVerse ScienceDirect

Computers in Biology and Medicine

journal homepage: www.elsevier.com/locate/cbm

Simulation of a pulsatile non-Newtonian flow past a stenosed 2D artery with atherosclerosis

Fang-Bao Tian [a], Luoding Zhu [b],*, Pak-Wing Fok [c], Xi-Yun Lu [d]

[a] Department of Mechanical Engineering, Vanderbilt University, 2301 Vanderbilt Place, Nashville, Tennessee 37235-1592, USA
[b] Department of Mathematical Sciences, Indiana University–Purdue University Indianapolis, 402 North Blackford Street, Indianapolis, Indiana 46202, USA
[c] Department of Mathematical Sciences, University of Delaware, 412 Ewing Hall, Newark, Delaware 19716, USA
[d] Department of Modern Mechanics, University of Science and Technology of China, 96 Jinzhai Road, Hefei, Anhui 230026, PR China

ARTICLE INFO

ABSTRACT

Atherosclerotic plaque can cause severe stenosis in the artery lumen. Blood flow through a substantially narrowed artery may have different flow characteristics and produce different forces acting on the plaque surface and artery wall. The disturbed flow and force fields in the lumen may have serious implications on vascular endothelial cells, smooth muscle cells, and circulating blood cells. In this work a simplified model is used to simulate a pulsatile non-Newtonian blood flow past a stenosed artery caused by atherosclerotic plaques of different severity. The focus is on a systematic parameter study of the effects of plaque size/geometry, flow Reynolds number, shear-rate dependent viscosity and flow pulsatility on the fluid wall shear stress and its gradient, fluid wall normal stress, and flow shear rate. The computational results obtained from this idealized model may shed light on the flow and force characteristics of more realistic blood flow through an atherosclerotic vessel.

© 2013 Published by Elsevier Ltd.

1. Introduction

Atherosclerosis is the main cause of heart attack and stroke, particularly in western developed countries. This disease causes a gradual stenosis of the lumen and hardening of the artery wall because of accumulation of lipids (e.g., low density lipoproteins or LDL) in the intima. The progressive build-up of deposits in the arterial wall may form a plaque that protrudes into the lumen and restricts the blood flow. In some cases a mature plaque may rupture suddenly without early warning and the broken plaque debris may block smaller arteries downstream. If the carotid artery (which supplies blood to the brain) is affected, one may suffer from stroke; if the coronary artery (which supplies blood to the heart) is affected, one may suffer from a heart attack. Currently the mechanism of plaque rupture is not clear despite a substantial amount of research [29]. Because the atherosclerotic plaque may project into the lumen from the wall, the blood flow in the lumen changes essentially from flow through a straight pipe to flow past an irregular obstacle. There are also corresponding changes in the

forces (shear and normal stresses) exerted by the flowing blood on the plaque surface. These altered forces may play an important role in the formation of fatty streaks or even in the rupture of more advanced lesions. Moreover, the altered flow and forces may directly affect the vascular endothelial cells lining the inner-most artery wall, or indirectly influence the vascular smooth muscle cells (SMCs) comprising the media.

The low wall shear stress (WSS) hypothesis was advocated by C.G. Caro et al. [5,6] in a series of papers and is a currently accepted theory for atherogenesis: low endothelial shear stress may decrease the secretion of arterial relaxing factor nitric oxide (NO) [7], promote inflammation through the secretion of chemoattractants [15] and increase endothelial permeability [21]. Generally, atherosclerotic lesions are observed in blood vessels that are bifurcated or highly curved.

While the most popular theory to explain atherogenesis is the low WSS theory (low wall shear stress initiates plaque build-up), competing theories suggest that other characteristics of the flow such as shear rate (SR) may be important [22]. Experiments by [39] on human umbilical vein monolayers show that endothelial cells migrate away from regions with high wall shear stress gradients (WSSGs) and have increased proliferation rates. This kind of behavior could drastically impact the permeability of the endothelium, enhance the transport of LDL into intima and initiate

plaque precursors. Forces exerted by the flowing blood on the endothelium may be decomposed into two perpendicular components: the component tangential to the endothelium (WSS), and the component normal to the endothelium (wall normal stress, or WNS). An increased WNS could impact plaque formation in several ways. First, increased WNS may stretch vascular SMCs residing in the media and Thubrikar [41] has shown that non-uniform stretching of SMCs could lead to vascular disease. Second, increased WNS means increased blood pressure (hypertension) which is a risk factor for strokes and heart attacks. Finally, higher WNS on the arterial wall may facilitate the deposition of LDL into the intima [4]. It is possible that high concentrations of LDL could lead to more oxidized LDL which could lead to plaque formation [16]. The combination of higher WNS and lower WSS (which could increase endothelial permeability) may produce additional synergistic effects.

There already exist many experimental and computational works that try to evaluate the fluid WSS on the plaque surface. Steinman et al. [35] investigated how stenotic geometry affects flow patterns by employing both concentric and eccentric carotid bifurcation models, assuming the same stenotic severity. Kohler et al. [24] investigated the WSS by using magnetic resonance imaging (MRI) measurements of the velocity field and comparing them with simulation results. Glickman et al. [2] conducted *in vitro* laboratory experiments of non-pulsatile flows through atherosclerotic carotid bifurcations. August et al. [1] examined the WSS in the carotid artery by computation and laboratory measurements. Teng et al. [40] studied critical flow shear stress and its association with plaque rupture using both *in silico* 3D models and *in vivo* MRI data. Stroud et al. [37] used modeling and simulation to study a 2D plaque model while Fischer et al. [17] introduced a new numerical method for the computational study of arterial blood flow with weak turbulence. Tan et al. [38] predicted the flow patterns in a carotid artery with atherosclerosis by using transitional variants and a two-equation model of turbulence. Grinberg et al. [20] investigated transient turbulence in a bifurcated carotid artery (built from MRI data) through high resolution simulations in three dimensions. Wong et al. [43] and Poepping et al. [32] performed *in vitro* studies on turbulence intensity in the downstream region of an arterial plaque. Chen et al. [8,10] studied the relationships between force/flow and the intimal hyperplasia (IH) in stented coronary arteries by computational and experimental approaches. All of these studies investigated the flow field (laminar or turbulent) and force field (mostly WSS) of blood flow past a stenosed 2D or 3D rigid artery (either obtained from MRI or idealized).

In this paper, we perform detailed numerical simulations of pulsatile/non-pulsatile and Newtonian/non-Newtonian blood flow past a localized stenosis in an idealized 2D blood vessel. It appears that there are generally fewer studies that address fluid WNS and flow SR associated with an atherosclerotic plaque. Therefore we include these two quantities in our studies in addition to the usual metrics of atherogenesis, WSS and WSSG. The goal is to perform a systematic parameter study to understand how flow profile, vessel geometry and plaque size affect WSS, WSSG, WNS and SR. To the best of our knowledge, such a systematic study is absent from the literature.

We would like to emphasize that similar to many existing studies, our work is based on the assumption that the artery is rigid and the flow is laminar. We do not use realistic vessel geometry from an actual patient (which may be obtained via MRI or ultrasound, as discussed above). Instead, we assume our domain to be a generic stenosed arterial segment which is compromised by atherosclerotic plaques of different severity. Our results may provide insight into the case of unsteady, high Reynolds number flow in a diseased artery and the associated

force fields. While the geometry of our problem is idealized, it nevertheless serves as a platform to study wall stresses in arteries with few branches, and potentially as a way to study the absorption of LDL and other macromolecules; for example Olgac et al. [31] use a similar idealized vessel geometry.

The remainder of the article is structured as follows: in Section 2 the mathematical formulation of the model problem of blood flow past a stenosed artery is given and the corresponding numerical method is briefly described. In Section 3 verification and validation of the simulation results are made. In Sections 4, 5 and 6 the major simulation results are presented and discussed. In Section 7 a summary and a discussion of our work are given.

2. Mathematical formulation and numerical method

Blood flow through a stenosed arterial segment with atherosclerosis can be modeled by an incompressible, viscous fluid with a viscosity that could be shear-rate dependent. We simulate the fluid through a 2D flow tunnel (with width $2a$ and length $25a$) with a stenosis taking the form $y = -a + A \exp[-(x-x_0)^2/b^2]$, where parameters A and b control the stenosis height and width, respectively, and x_0 is the center of the stenosis. Fig. 1 shows the geometry of the model problem with seven different stenoses to represent plaques of different size and shape. A velocity profile $U(y, t)$ is given at the inlet (left boundary) to model the pulsatile flow.

The fluid dynamics is governed by the incompressible Navier–Stokes equations,

$$\rho\left(\frac{\partial \mathbf{u}}{\partial t} + \mathbf{u} \cdot \nabla \mathbf{u}\right) = -\nabla p + \nabla \cdot \mathbf{S}, \tag{1}$$

$$\nabla \cdot \mathbf{u} = 0, \tag{2}$$

where ρ is the density, p is the pressure, $\mathbf{u}$ is the velocity, and $\mathbf{S} = 2\eta\mathbf{D}$ with $\mathbf{D} = (\nabla\mathbf{u} + \nabla\mathbf{u}^T)/2$. For a Newtonian fluid, $\eta/\rho = \nu$, and the Reynolds number is defined by $Re = a\overline{U}/\nu$ with $\overline{U}$ being the averaged incoming velocity. For a non-Newtonian fluid, the viscosity is shear rate dependent $\eta = \eta(\dot{\gamma})$. In our work the Carreau–Yasuda model [18,19] is used where the viscosity of the blood is described by

$$\eta = \eta_\infty + (\eta_0 - \eta_\infty)[1 + (\lambda\dot{\gamma})^{a_0}]^{(n-1)/a_0}, \tag{3}$$

where $\dot{\gamma}$ is the flow shear rate which is defined by $\dot{\gamma} = \sqrt{2D_{ij}D_{ij}}$ with $D_{ij} = (u_{i,j} + u_{j,i})/2$. The Reynolds number for the non-Newtonian fluid can be defined as $Re = \rho a\overline{U}/\eta(0)$. The Navier–Stokes equations together with the Carreau–Yasuda model have been used for modeling and simulation of blood flows in the literature and very good agreements between computational results and laboratory measurements have been found [18,19,12–14].

A fractional-step velocity correction method [25] is used to solve Eqs. (1) and (2). The discretized form can be obtained by splitting Eq. (1) into two substeps as,

$$\hat{\mathbf{u}} = \mathbf{u}^n + \Delta t(\eta\nabla^2\mathbf{u}^n/\rho + \nabla\eta \cdot (\nabla\mathbf{u}^n + (\nabla\mathbf{u}^n)^T)/\rho - \mathbf{u}^n \cdot \nabla\mathbf{u}^n), \tag{4}$$
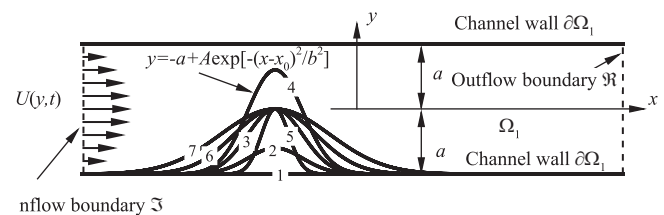

Fig. 1. Schematic representation of a 2D stenosed artery. The geometrical parameters are: (1) $A/a = 0$ (channel flow), (2) $A/a = 0.4$ and $b/a = 1.0$, (3) $A/a = 1.0$ and $b/a = 1.0$, (4) $A/a = 1.6$ and $b/a = 1.0$, (5) $A/a = 1.0$ and $b/a = 0.5$, (6) $A/a = 1.0$ and $b/a = 1.5$, and (7) $A/a = 1.0$ and $b/a = 2.0$.

$$\mathbf{u}^{n+1} = \hat{\mathbf{u}} - \frac{\Delta t \nabla p^{n+1}}{\rho}, \tag{5}$$

where $\hat{\mathbf{u}}$ is an intermediate velocity, Δt is the time-step, and superscripts n and $n+1$ represent the time levels. In the splitting method, it is required that the velocity field $\mathbf{u}^{n+1}$ satisfies the incompressibility constraint, i.e. Eq. (2). Apply the divergence operator on both sides of Eq. (5), and using Eq. (2), we obtain the pressure Poisson equation,

$$\nabla^2 p^{n+1} = \frac{\rho \nabla \cdot \hat{\mathbf{u}}}{\Delta t}. \tag{6}$$

Eqs. (4)–(6) are solved subject to the boundary conditions,

$$\mathbf{u} = 0, \quad (x, y) \in \partial \Omega_1, \tag{7}$$

$$\mathbf{u} = (U(y, t), 0), \quad (x, y) \in \Im, \tag{8}$$

$$\mathbf{T} = 0, \quad (x, y) \in \Re, \tag{9}$$

where $U(y, t)$ is the velocity profile of a Poiseuille flow and $T_{i,j} = -p\delta_{ij} + \eta(u_{i,j} + u_{j,i})$ is the stress. The flow may be steady if the inlet velocity $(U(y,t), 0)$ is time independent, or pulsatile if $(U(y,t), 0)$ is periodic in time, i.e., $U(y, t + T) = U(y, t)$. Eqs. (4)–(6) are discretized by a finite element approach using the Galerkin weighted residual method. In the present work, three-node triangular isoparametric elements are used. Near the stationary boundaries (upper and lower walls), more elements are used to resolve boundary layers and associated vortices. On each element, piecewise-continuous bilinear basis functions are used for u, v, p, and η. The resultant linear system of algebraic equations is solved by Successive-Over-Relaxation (SOR). A summary of the algorithm is as follows: (1) Given the values of all variables at time level n, calculate the intermediate velocity $\hat{\mathbf{u}}$ by Eq. (4); (2) Solve the pressure at time level $n+1$ using Eq. (6) with the following boundary conditions: $p=0$ at the outlet and $\partial p/\partial n = 0$ on all of the other boundaries; (3) Update the velocity at time level $n+1$ through Eq. (5). See Kovacs and Kawahara [25] for further technical details.

The physical parameters are listed in Table 1, which are the same as in Ref. [31]. For most cases, $Re = \rho U_0 a/\eta = 199.8 \approx 200$. The governing equations and the boundary conditions are rendered dimensionless using ρ, U_0 and a. The fluid stress on the wall is an important quantity that we will study. From Ref. [44], it is known that the stress on the wall is,

$$\mathbf{f} = -p\mathbf{n} + \eta\boldsymbol{\omega} \times \mathbf{n}, \tag{10}$$

where $\mathbf{n}$ is the normal vector of the wall, $\boldsymbol{\omega} = \nabla \times \mathbf{u}$ is the vorticity. In addition, $\mathbf{n} \cdot \mathbf{f}$ is the WNS and $\boldsymbol{\tau} \cdot \mathbf{f}$ (with $\boldsymbol{\tau}$ being the tangent vector of the wall) is the WSS. Considering Eq. (10), we have the WNS and WSS for two-dimensional flow as

$$\mathbf{n} \cdot \mathbf{f} = -p, \tag{11}$$

$$\boldsymbol{\tau} \cdot \mathbf{f} = \eta\boldsymbol{\tau} \cdot (\boldsymbol{\omega} \times \mathbf{n}) = -\eta\omega. \tag{12}$$

We would like to point out that (1) because the pressure is computed up to an arbitrary constant from the Navier–Stokes equations, the WNS computed in our work may differ by a constant from the actual physiological situation. Equating the computed value to the known physiological value at a single point

by adding or subtracting a constant gives us the physiological value of the WNS in the whole computational domain. We do not try to do this because the gradient of the WNS is uniquely determined and sometimes the gradient is more important; (2) the WSS is directional, but it is its magnitude that is more of biological relevance. Therefore in our work the WSS is calculated by $\eta|\omega|$, and the gradient of WSS (WSSG) is then obtained by $d(\eta|\omega|)/ds$, where s is the arc length along the wall.

To compare with our simulation results, the physiological range of the WSS, WSSG, WNS, and SR are given as follows. Healthy WNS in human upper extremity can be estimated from blood pressure which is typically: 80-120 mmHg e.g. see Levick [27]. Shear Stress on the endothelium in human arteries is estimated to be 0.5–1.5 Pa [27]. Peak/mean shear rates in human brachial arteries were found to be 908/85 s^{-1} in [36]. Finally, *in vitro* experiments on human umbilical vein monolayers [39] use shear stress gradients of up to 34 dyne/cm^2 per mm. Our computational results for these quantities when converted back to dimensional form are consistent with these normal ranges when the degree of stenosis in the vessel is low.

3. Verification and validation

The method and code used here for our current problem has been validated carefully in previous works and applied with success to a wide range of flow problems [28,30,34]. The main difference between the method and code we use here and those used in these references is the method for solving the resultant linear system (Gauss–Seidel was used in the references and SOR is used in our work). To make sure the numerical results are reliable, verification and validation of the numerical method and its implementation are further carried out by three approaches. First, the code implementing the method is used to simulate a laminar flow through a channel and the computational results are compared with the analytical solution. Secondly, mesh and time-step size independence studies are performed on the model problem of interest. Finally, comparisons of our simulation results on the model problem and on non-Newtonian flow through a contracting 3D channel with existing results (computational and experimental) from literature are made to show the correctness of the method and code.

3.1. Laminar flow in a channel

Consider the two-dimensional laminar flow of an incompressible Newtonian fluid in a channel of height $2a$ with a Poiseuille profile at the inlet as shown in Fig. 1 (case 1). In the simulation, the initial condition and the boundary conditions are set as,

$$u(x, y) = v(x, y) = p(x, y) = 0, \quad (x, y) \in \Omega_1, t = 0,$$

$$u(x, y) = U(y) = U_0(a^2 - y^2), v = 0, \quad (x, y) \in \Im, t > 0,$$

$$u(x, y) = v(x, y) = 0, \quad (x, y) \in \partial\Omega_1, t > 0,$$

$$p(x, y) = 0, \quad (x, y) \in \Re, t > 0.$$

The computation is carried out for a domain size of $15a \times 2a$. The total number of nodes is approximately 1.6×10^4, the total number of element is approximately 2.6×10^4 and the time step size is 5×10^{-4}. The fully developed velocity profile computed by the numerical simulation is compared to the analytical solution $u(y) = 1 - y^2$ where y in $[-1, 1]$, and an excellent agreement is found.

Table 1
Physical parameters.

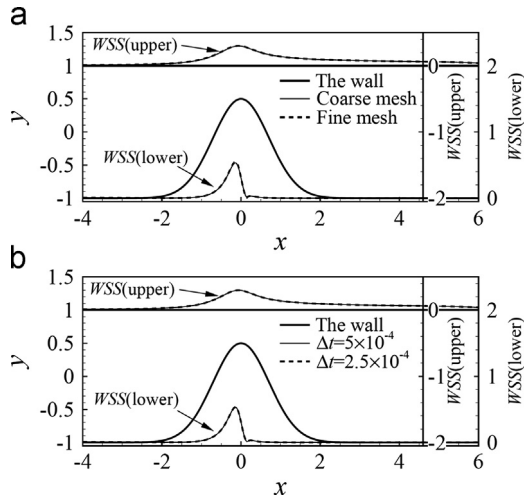| ρ	μ	$U_0(U_{max})$	a
1.05 g/cm^3	0.0035 Pa s	36 cm/s	0.185 cm

Fig. 2. Wall shear stress (WSS) on the top and bottom walls: (a) comparison between coarse and fine meshes; (b) comparison between larger and smaller time-steps.

Fig. 3. Comparison: the present numerical result of WSS and the analytical solution.

3.2. Grid independence and time-step independence studies

For a fixed domain size and a fixed set of parameters, two simulations are carried out by using two sets of non-uniform unstructured meshes: a coarser mesh (the total node number is approximately 1.6×10^4, the total element number is approximately 2.6×10^4) and a finer mesh (the total node number is approximately 2.3×10^4, the total element number is approximately 4.5×10^4). In both cases, $Re = 200$, $A/a = 1.5$, $b/a = 1$, and $\Delta t = 5 \times 10^{-4}$. The WSS on the upper and lower walls is shown in Fig. 2(a). It can be seen from the figure that the WSS computed on the coarser grid agrees very well with that computed on the finer grid and the maximum difference in the WSS is less than 2.5%. Therefore, the coarser mesh is considered to be sufficiently fine to resolve the flow in space and will be used for all of the simulations reported in the paper. To study the time-step size independence, we perform an additional simulation on the coarser mesh with $\Delta t = 2.5 \times 10^{-4}$. All other parameters are the same as those used in the grid independence study. The computational results from the two time-step sizes are plotted in Fig. 2(b) for comparison. As we can see in the figure, the WSS computed with $\Delta t = 5 \times 10^{-4}$ agrees very well with that computed from $\Delta t = 2.5 \times 10^{-4}$, and the maximum difference in the WSS is less than 0.035%. Therefore $\Delta t = 5 \times 10^{-4}$ is considered to be sufficiently small to resolve the flow in time and will be used for all the simulations reported in the paper.

3.3. Comparison with analytical solution and existing results in literature

The lower panel of Fig. 3 shows the geometry of the flow channel. The upper panel shows the distribution of WSS along the lower wall (solid) and the analytical WSS for a straight channel (dashed). We see that the computed WSS on the stenosed channel approaches the analytical solution downstream of the stenosis. The computed WSS looks similar to the predicted WSS in [31]. The parameters used in these two simulations are the same. However, the plaque was assumed to be axi-symmetrical in [31]; therefore the magnitude of WSS is greater than in our case.

To validate our computational results of non-Newtonian flow using the Carreau–Yasuda model, we performed simulations of non-Newtonian fluid flow through a gradually contracting 3D channel which is a case where laboratory data are available from the literature. See Fig. 4 for the middle plane (x–y plane) of the
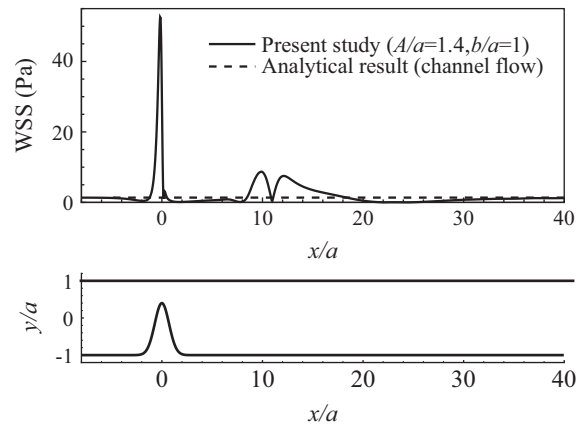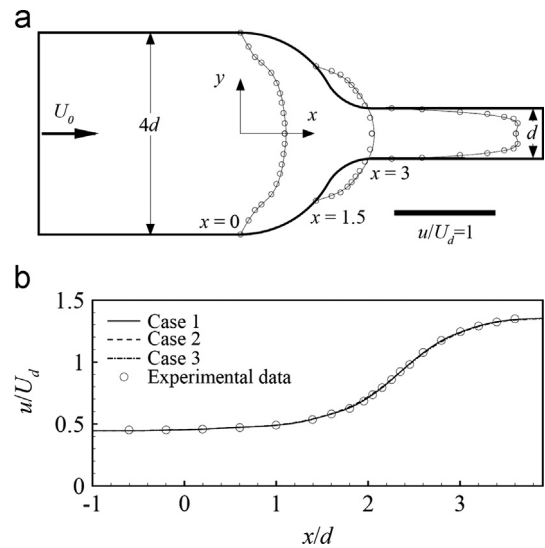

Fig. 4. Velocity profiles: (a) along the y-direction and (b) along the central line. Case 1: 4×10^4 elements, $\Delta = 5 \times 10^{-4}$; Case 2: 6×10^4 elements, $\Delta = 5 \times 10^{-4}$; Case 3: 4×10^4 elements and $\Delta = 2.5 \times 10^{-4}$.

3D channel. The contraction ratio along the y-direction is 4:1. The dimension along the z-direction (perpendicular to the page) is $4d$ and no contraction is made along the other two directions. See Keegan [23] for more details. The parameters for the Carreau–Yasuda model used in the laboratory experiments were $\rho = 1000$ kg/m^3, $\mu_0 = 0.073$ kg/ms, $\mu_\infty = 0.0025$ kg/ms, $a = 0.52$, $\lambda = 0.45$ s and $n = 0.61$. The Re based on the downstream duct height d and velocity at the end of the contraction U_d is 30. The upper panel in Fig. 4 shows the x-component of the velocity $u(y)$ at three different locations along the x-direction on the middle plane of the duct: one before the contraction, one after the contracted portion, and the third in the contraction. The dark line depicts the middle plane of the duct. The circles represent data from laboratory measurements, which agree very well with the thin lines from our computational results.

The lower panel of Fig. 4 shows the results of mesh and time step size refinement. It shows the x-component of the velocity $u(y)$ on the middle line of the middle plane. There are three over-lapping curves on the figure corresponding to three simulations using different number of elements and time step size: Case (1) uses 4×10^4 elements and $\Delta t = 5 \times 10^{-4}$; Case (2) uses 6×10^4 elements and $\Delta t = 5 \times 10^{-4}$; Case (3) uses 4×10^4 elements and $\Delta t = 2.5 \times 10^{-4}$. These three computational results agree very

well with one another. This indicates that our numerical results are independent of the grid width and time step size. Therefore we believe that the number of elements and time steps in our simulations are sufficient to resolve the flow. Again, the circles on the figure represent the laboratory data and the agreement is excellent.

4. Effects of stenosis (*A* and *b*)

The size and shape of an atherosclerotic plaque may vary significantly from patient to patient, from location to location for a given patient, and may also change with time, e.g. the plaque may grow from a fatty streak (a slight stenosis) to a mature plaque
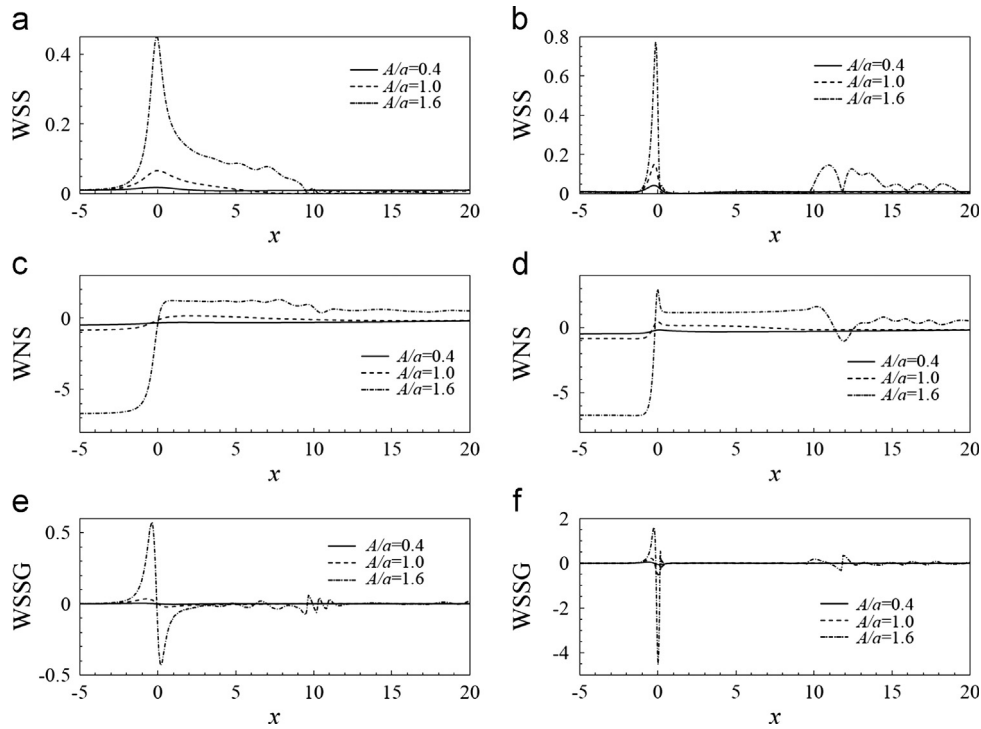

Fig. 5. Wall shear stress (WSS), wall shear stress gradient (WSSG) and WNS on the top and bottom walls for different A/a at $b/a = 1.0$: (a), (c) and (e) are the WSS, WNS, and WSSG at the top wall; (b), (d) and (f) are the WSS, WNS, and WSSG at the bottom wall.
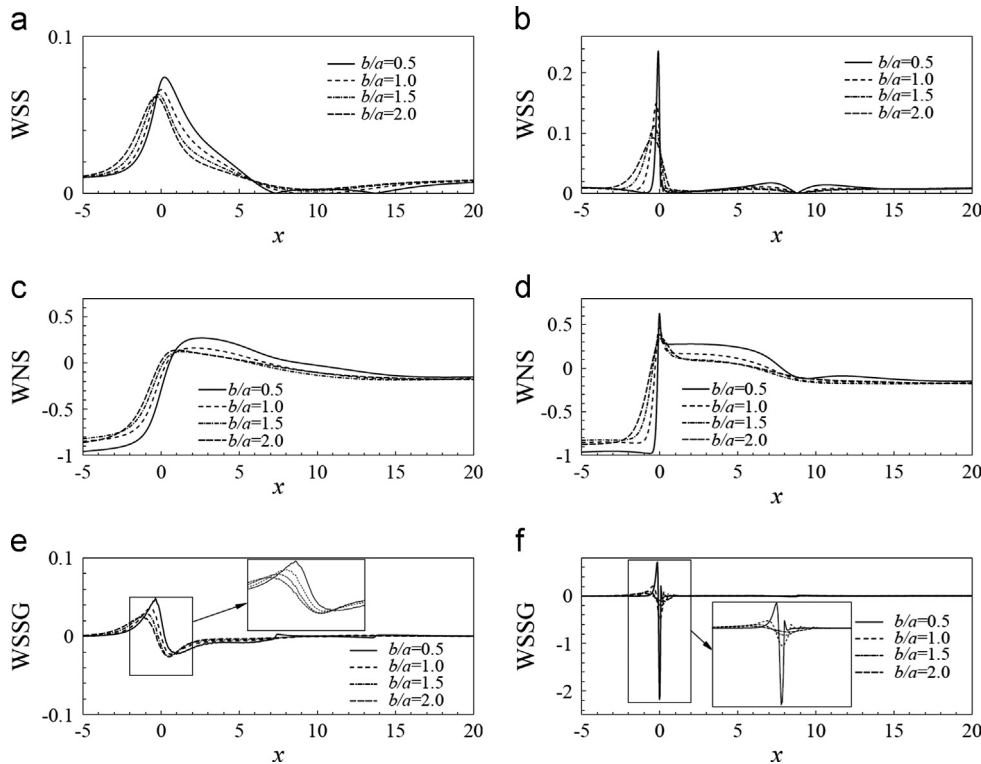

Fig. 6. Wall shear stress (WSS), wall shear stress gradient (WSSG) and WNS on the top and bottom walls for different b/a at $A/a = 1.0$: (a), (c) and (e) are the WSS, WNS, and WSSG at the top wall; (b), (d) and (f) are the WSS, WNS, and WSSG at the bottom wall.

(a severe stenosis) that causes severe blockage of the lumen. Plaques of different size and shape will change the flow profile. In particular, it is of interest to know how the WSS and its gradient (WSSG), WNS, and flow SR change with the geometry of the plaque. Note that in the following figures, the plot of flow SR is not given because the distribution of the SR along the upper/lower walls is similar to that of the WSS (except the effect of Reynolds numbers). Although their absolute values are significantly different. Instead the contours of SR on the whole flow domain are given where the strength of the flow shear rate can be seen clearly.

To study the geometric effect of a plaque, we have run a series of simulations by systematically varying A/a (characterizing the height of the plaque) from 0.4 to 1.6 and b/a (characterizing the width of the plaque) from 0.5 to 2.0. The Reynolds number is 200. The main results are plotted in Figs. 5 and 6. In both figures the left group corresponds to the upper wall and the right group corresponds to the lower wall. The first row in the figures shows the WSS, the second row shows the WNS (i.e., pressure in our case), and the third row shows the WSSG. From Fig. 5 we can see that: (1) the greater A/a, the larger the WSS, WSSG, and SR on both the upper and lower walls, (2) the WSSG magnitude attains its maximum near the stenosis on the downstream side, (3) the WSS, WSSG, and SR are all smaller on the upper wall than on the lower wall, (4) the pressure is lower on the upstream side of the stenosis and higher on the downstream side of the stenosis and its absolute value increases with the value of A/a on both walls, (5) significant oscillations in WSS, WSSG, WNS, and SR can be seen on the lower wall downstream, far away from the stenosis.

It is interesting to point out that while a disturbance in part of a flow domain (such as a stenosis on the lower wall) affects the magnitudes of WSS, WSSG, and SR on both walls, the degree of influence is different: in particular, the lower wall experiences substantially greater WSSG and some research [39] has shown that endothelial cells become more permeable to macromolecules under large stress gradients. The implication is that endothelial surfaces subject to higher WSSG may be more susceptible to atherosclerosis.

Now that we have seen from Fig. 5 the influence of the height of the disturbance, now let us look at the influence of its width b/a for a fixed $A/a=1$. A series of simulations with different values of b/a are run and the results are shown in Fig. 6. From this figure we can see that the width of the stenosis has a similar effect as its height on WSS, WNS, WSSG, and SR: small values of b/a, cause significantly greater WSS, WSSG, and SR while larger values of b/a results in a smoother change of WSS and its gradient. Again the bottom wall experiences more dramatic changes as the stenosis becomes more acute compared to the top wall. Interestingly a cusp occurs in the graphs of WSS, WNS, and SR downstream of the stenosis. Comparison of these two figures (Figs. 5 and 6), indicates that the variable A/a (stenosis height) has a substantially greater effect on WSS, WNS, WSSG, and SR than the variable b/a (stenosis breadth), i.e. plaque height is much more influential on the hemodynamics than breadth. The severity of an atherosclerosis plaque is in general gauged by the percentage of blockage of the lumen which is mainly caused by its height rather than its breadth. Our results may explain why this criterion in categorizing plaque burden is used in practice.

Fig. 7 shows the streamlines (SLs), contours of flow shear rate (SR) and vorticity (VO) for four typical cases in Figs. 5 and 6. The top left group (three panels) corresponds to the SL, SR, and VO for the case with $A/a=0.4$ and $b/a=1.0$. The top right group corresponds to the case with $A/a=1.6$ and $b/a=1.0$. Similarly, the
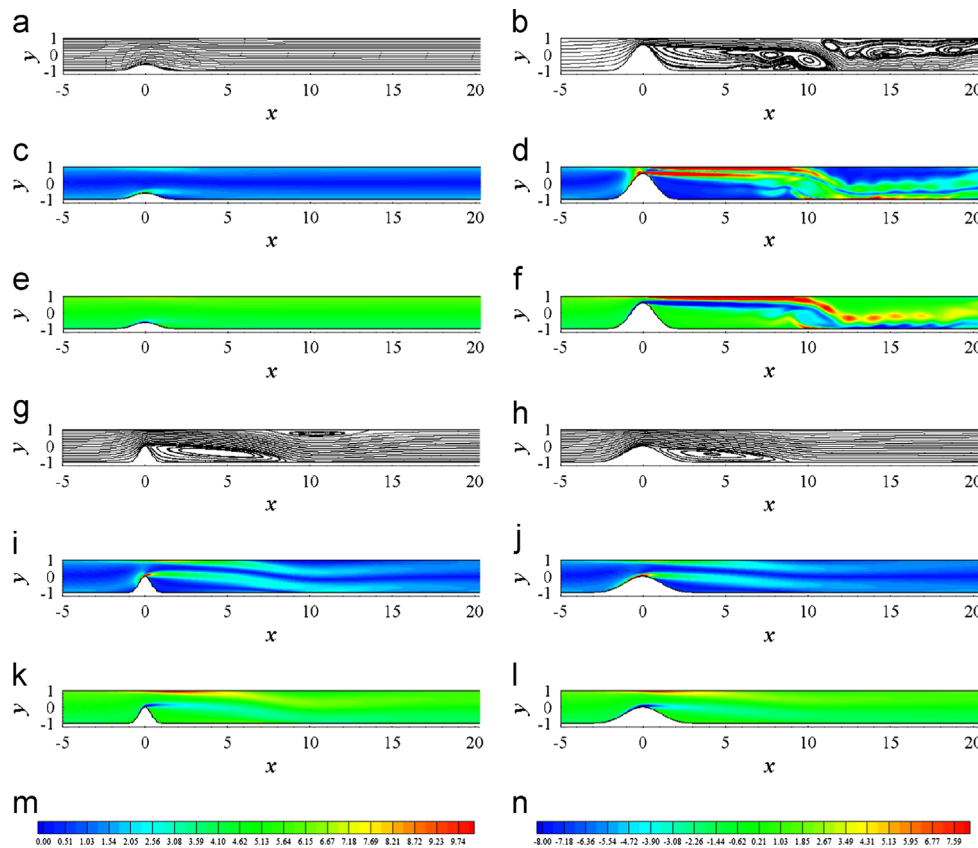

Fig. 7. The streamline (SL), shear rate (SR) and vortex (VO). (m) and (n) are the contour legends for SR and VO, respectively. All the contour figures in this paper have the same contour legends. (a) SL: $A/a=0.4$ and $b/a=1.0$, (b) SL: $A/a=1.6$ and $b/a=1.0$, (c) SR: $A/a=0.4$ and $b/a=1.0$, (d) SR: $A/a=1.6$ and $b/a=1.0$, (e) VO: $A/a=0.4$ and $b/a=1.0$, (f) VO: $A/a=1.6$ and $b/a=1.0$, (g) SL: $A/a=1.0$ and $b/a=0.5$, (h) SL: $A/a=1.0$ and $b/a=1.5$, (i) SR: $A/a=1.0$ and $b/a=0.5$, (j) SR: $A/a=1.0$ and $b/a=1.5$, (k) VO: $A/a=1.0$ and $b/a=0.5$, (l) VO: $A/a=1.0$ and $b/a=1.5$, (m) Contour legend of SR, and (n) Contour legend of VO.

bottom left corresponds to the case $A/a=1.0$ and $b/a=0.5$, and the bottom right corresponds to the case $A/a=1.0$ and $b/a=1.5$. The top two groups illustrate the influence of stenosis geometry (both height and width) on the streamlines, contours of shear rate and vortices. One can see from comparison of the top left and top right groups that the stenosis height may have significant influence on the downstream flow: when A/a is very large (e.g. 1.6 which may correspond to a 80% lumen blockage), the recirculation zone behind the stenosis is stretched to approximately 12 times of the channel half-width (corresponding to the lumen radius) and there exists a second recirculation zone near the top wall downstream of the first recirculation zone. Underneath the second zone exists a vortex street which may explain the oscillations observed in Fig. 5. The two zones are separated by a narrow gap. One can also see that the flow shear rate and the vorticity behind the tall stenosis is significantly increased and concentrated near the top wall behind the stenosis. The substantially elevated shear rate and vorticity intensity could cause damage to circulating blood cells such as erythrocytes and the glycocalyx covering the vascular endothelial cells on the artery wall. By comparison of the remaining two groups we can see that the stenosis width has similar but weaker effect as the stenosis height on the downstream flow. Notice that when the stenosis is sufficiently tall, a second recirculation zone appears near the top wall after the first recirculation zone behind the stenosis (see the bottom left group). This again suggests that a highly concentrated stenosis (with a very small value of b/a) has a similar effect on the flow as a tall stenosis (large value of A/a).

5. Effects of *Re*

Fig. 8 shows the effect of Reynolds number on the WSS, WNS and WSSG for four typical values ($Re=100, 200, 300, 400$) with $A/a=b/a=1.0$. This figure shows that as the Reynolds number increases in the range 100 to 400, the WSS and its gradient on both

top and bottom walls decreases, the (signed) WNS on both walls increases, and the flow shear rate SR (not shown here) increases near the stenosis and varies in a more complicated way far downstream. When the Reynolds number is large enough, the WSS, WNS, WSSG, and SR profiles on the lower wall all feature a cusp near $x=10$. This is probably caused by the presence of recirculation zones downstream. (See figures of streamlines.)

6. Non-Newtonian effects

The Carreau–Yasuda model is now used to model the blood rheology. The shear-thinning viscosity of the blood is described by

$$\eta = \eta_\infty + (\eta_0 - \eta_\infty)[1 + (\lambda\dot{\gamma})^{a_0}]^{(n-1)/a_0}, \tag{13}$$

where $\dot{\gamma}$ is the shear rate defined by $\dot{\gamma} = \sqrt{2D_{ij}D_{ij}}$ with $D_{ij} = (u_{i,j} + u_{j,i})/2$. In our simulations, $\eta_0 = 22 \times 10^{-3}$ Pa. s, $\eta_\infty = 2.2 \times 10^{-3}$ Pa s, $\lambda = 0.110$ s, $a_0 = 0.664$ and $n = 0.392$. The Reynolds number of the non-Newtonian flow is defined using the viscosity at zero shear rate:

$$Re = \frac{\rho a \overline{U}}{\eta_0}, \tag{14}$$

where $\overline{U}$ is the average velocity. In our study $Re=200$ for the non-Newtonian case.

6.1. Non-Newtonian fluid with steady incoming flow

Non-Newtonian effects on WSS, WNS, and WSSG are shown in Figs. 9 and 10. We can see from these two figures that compared to Newtonian case, the non-Newtonian fluid case has lower WSS and gradient, and higher flow shear rate on both the top and bottom walls. This is caused by the shear-thinning property of the fluid. Shear-thinning results in smaller effective fluid viscosity wherever the flow shear rate is higher, i.e. higher effective local Reynolds
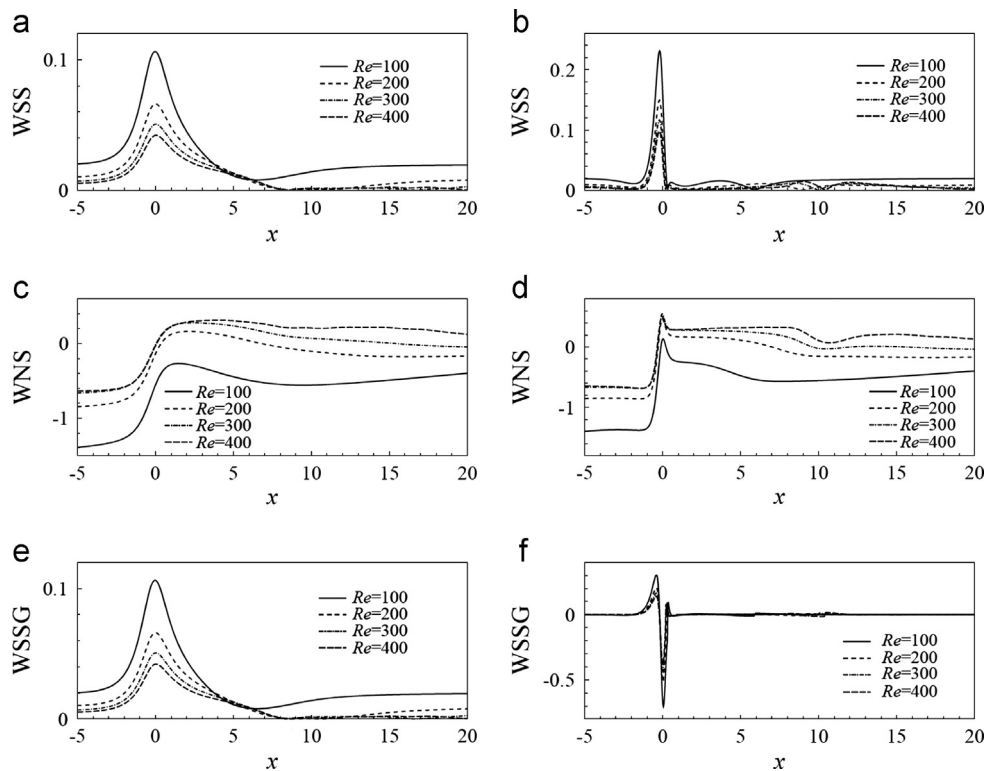

Fig. 8. Wall shear stress (WSS), wall shear stress gradient (WSSG) and WNS on the top and bottom walls for different *Re* at $A/a=1$ and $b/a=1.0$: (a), (c) and (e) are the WSS, WNS, and WSSG at the top wall; (b), (d) and (f) are the WSS, WNS, and WSSG at the bottom wall.
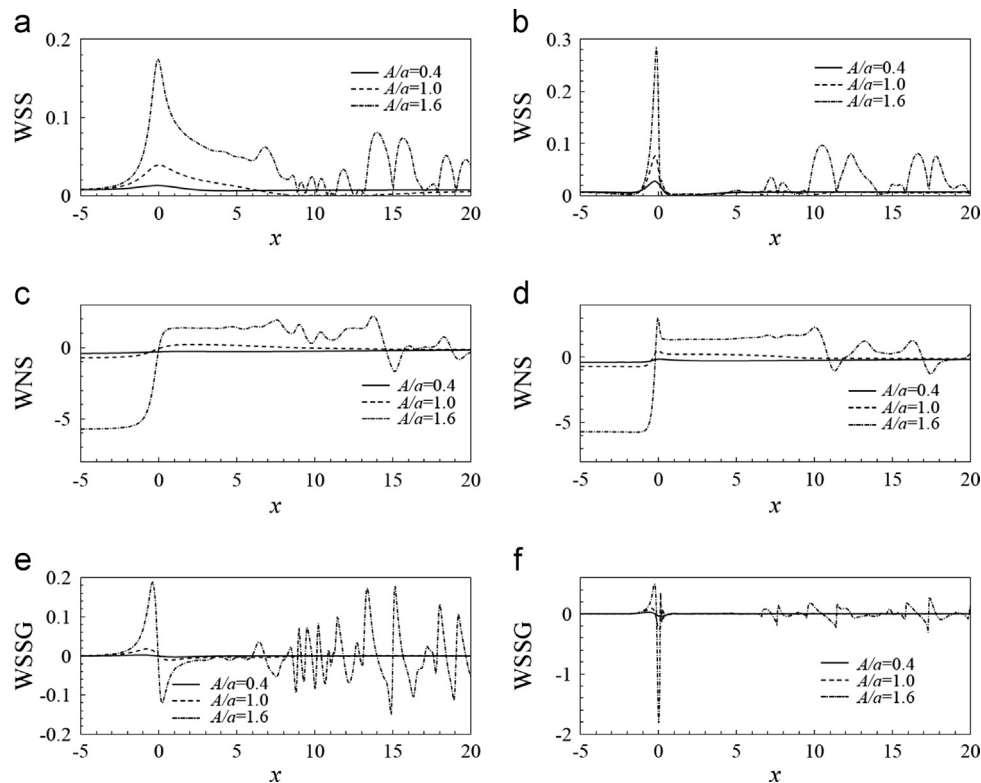
Fig. 9. Non-Newtonian flow: wall shear stress (WSS), wall shear stress gradient (WSSG), and WNS on the top and bottom walls for different A/a at $b/a=1.0$. (a), (c) and (e) are the WSS, WNS, and WSSG at the top wall; (b), (d) and (f) are the WSS, WNS, and WSSG at the bottom wall.
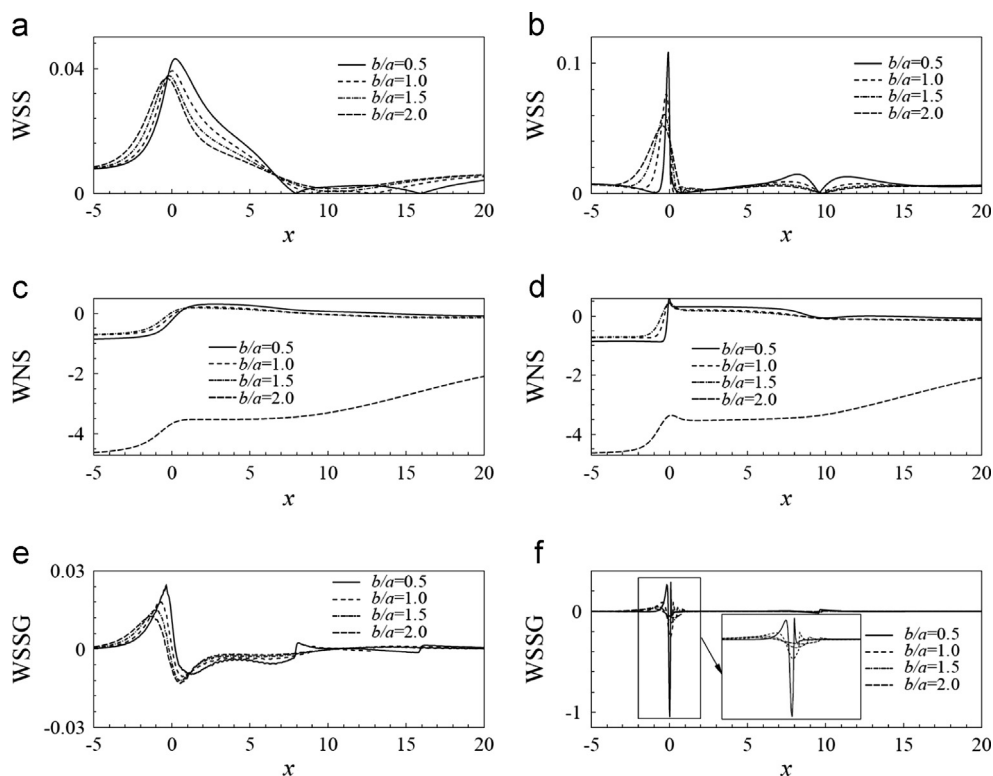

Fig. 10. Non-Newtonian flow: wall shear stress (WSS), wall shear stress gradient (WSSG), and WNS on the top and bottom walls for different b/a at $A/a=1.0$. (a), (c) and (e) are the WSS, WNS, and WSSG at the top wall; (b), (d) and (f) are the WSS, WNS, and WSSG at the bottom wall.

number. This is perhaps the reason why shear-thinning fluids have behaved similarly to Newtonian fluids under a higher Reynolds number. Most of the WSS, WNS, WSSG, and SR distributions downstream from the plaque center are highly oscillatory beyond

the recirculation zone. The oscillations in this region can be explained by the next figure showing the flow field.

Fig. 11 for the non-Newtonian fluid is similar to Fig. 7 for the non-Newtonian fluid. Compared to the Newtonian case, the
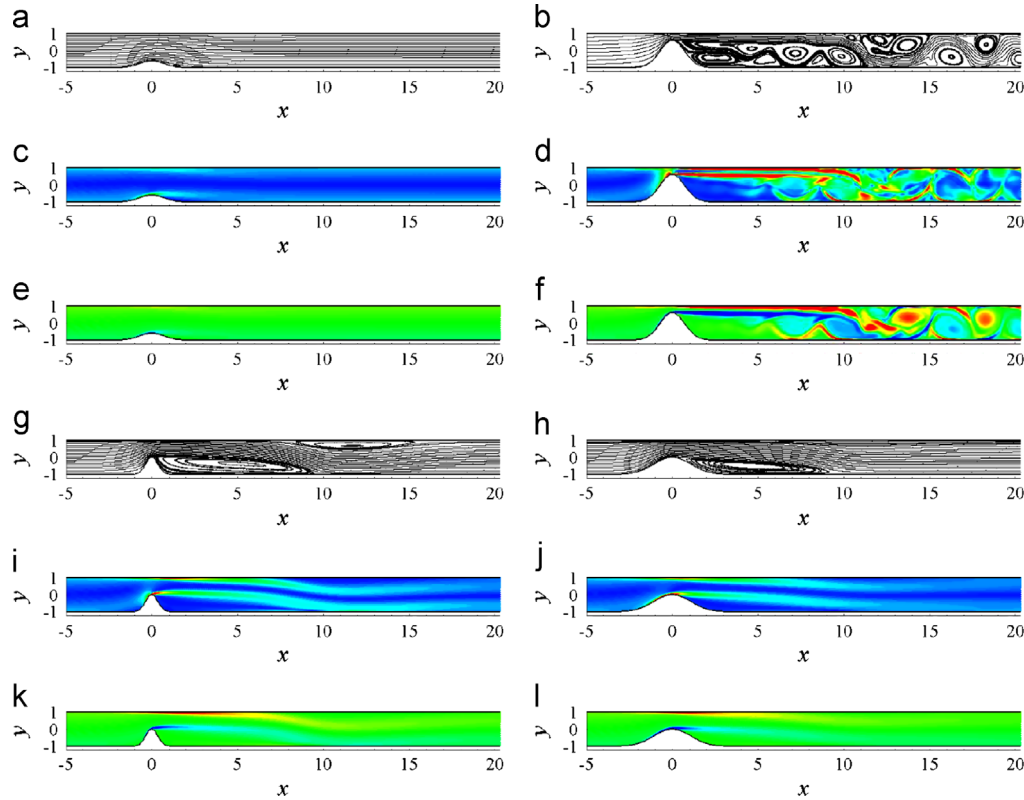
Fig. 11. The streamline (SL), shear rate (SR) and vortex (VO) for Non-Newtonian. (a) SL: $A/a = 0.4$ and $b/a = 1.0$, (b) SL: $A/a = 1.6$ and $b/a = 1.0$, (c) SR: $A/a = 0.4$ and $b/a = 1.0$, (d) SR: $A/a = 1.6$ and $b/a = 1.0$, (e) VO: $A/a = 0.4$ and $b/a = 1.0$, (f) VO: $A/a = 1.6$ and $b/a = 1.0$, (g) SL: $A/a = 1.0$ and $b/a = 0.5$, (h) SL: $A/a = 1.0$ and $b/a = 1.5$, (i) SR: $A/a = 1.0$ and $b/a = 0.5$, (j) SR: $A/a = 1.0$ and $b/a = 1.5$, (k) VO: $A/a = 1.0$ and $b/a = 0.5$, and (l) VO: $A/a = 1.0$ and $b/a = 1.5$.
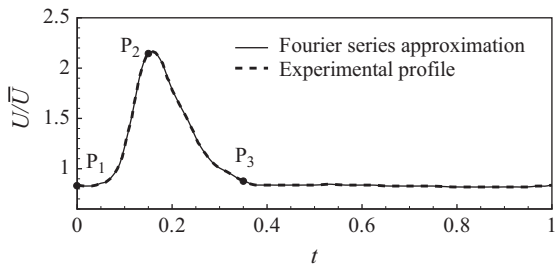

Fig. 12. Mean incoming velocity during the pulse cycle.

non-Newtonian flow is similar in general for most stenoses parametrized by different A/a and b/a. The non-Newtonian effects are significant only for a severe stenosis: plaques with very large A/a and very small b/a. In these cases (e.g., the top right group of Fig. 11), the flows in front of the plaque still look similar, but flows behind the plaque are qualitatively different: the flows are now more structured/ordered in the Newtonian case but more chaotic/disordered in the non-Newtonian case. This discernable difference may, again, be explained by the shear-thinning property of the fluid. A precipitous obstacle (e.g. a tall and narrow stenosis) can significantly disturb the flow. The disturbances can greatly increase the shear rate in the flow which locally alters the effective fluid viscosity. Large spatial and temporal gradients in the viscosity generate rich phenomena and fast variations in the flow dynamics.

6.2. Newtonian fluid with pulsatile incoming flow

Arterial blood flow is pulsatile. The pulsatility is generated by the intermittent motion of the heart, i.e. the systolic and diastolic phases of a heartbeat. Hence the blood flow is both highly

unsteady (within a heartbeat) and quasi-periodic (at least in theory) from one heartbeat to the next. Therefore, here we study the influence of the pulsatility on the flow characteristics, focusing on WSS and WNS since flow SR varies in the same fashion as the WSS (although their magnitudes differ significantly) and WSSG may be gauged directly from the WSS. We first look at the pulsatile effect on Newtonian flows, and then on non-Newtonian flows. The flow waveform used in experiments by [19] is applied at the inlet. We use Fourier series to approximate the experimental profile, as shown in Fig. 12.

Because the flow is time-dependent within the period of a heartbeat (T) which is the reciprocal of the heartbeat frequency (normal range 60–90 Hz), to show the unsteadiness of the flow, three typical time instants, marked by P_1, P_2, and P_3 in Fig. 12, are chosen: one instant corresponding to the beginning of the systolic phase (P_1), the second one corresponding to the end of the systolic phase (P_2), and the last one corresponding to a time instant near the end of the diastolic phase. Figs. 13 and 14 show the WSS versus longitudinal distance x on upper and lower walls for different values of A/a and b/a for the three time instants. In both figures, the left column shows the WSS on the top wall and the right column shows the WSS on the bottom wall; the top row corresponds to P_1, the middle row corresponds to P_2, and the last row corresponds to P_3. Compared to the non-pulsatile cases (Figs. 5 and 6), we see significantly more oscillations in the WSS on both top and bottom walls. Presumably the increased variation in WSS is caused by the flow pulsatility and unsteadiness. Also we notice that the WSS distributions are similar at instants P_1 and P_2, but both are very different at instant P_3 when the magnitudes of WSS are significantly greater. Intuitively one may speculate that the WSS reaches its maximum at P_2, i.e. near the end of the systolic phase, since after that point the flow gradually slows down. However, according to our simulation, the WSS attains its
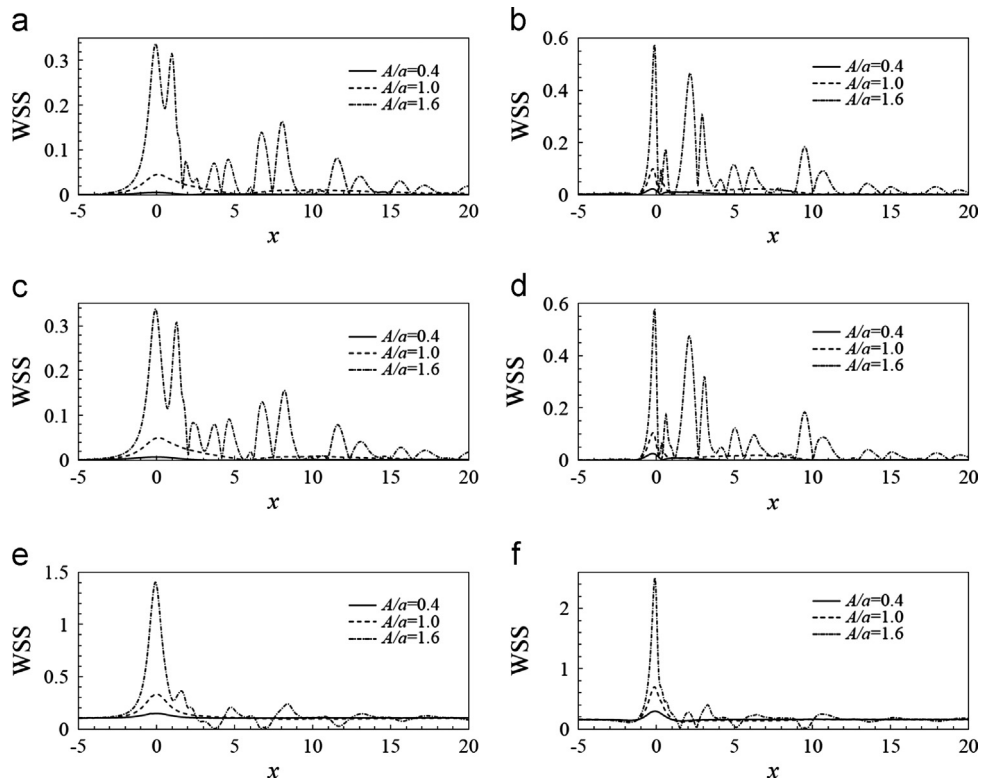
Fig. 13. WSS of Newtonian pulsatile flow on top (left) and bottom (right) walls at P_1 [(a) and (b)], P_2 [(c) and (d)], and P_3 [(e) and (f)] for different values of A/a.

Fig. 14. WSS of Newtonian pulsatile flow on top (left) and bottom (right) walls at P_1 [(a) and (b)], P_2 [(c) and (d)], and P_3 [(e) and (f)] for different values of b/a.
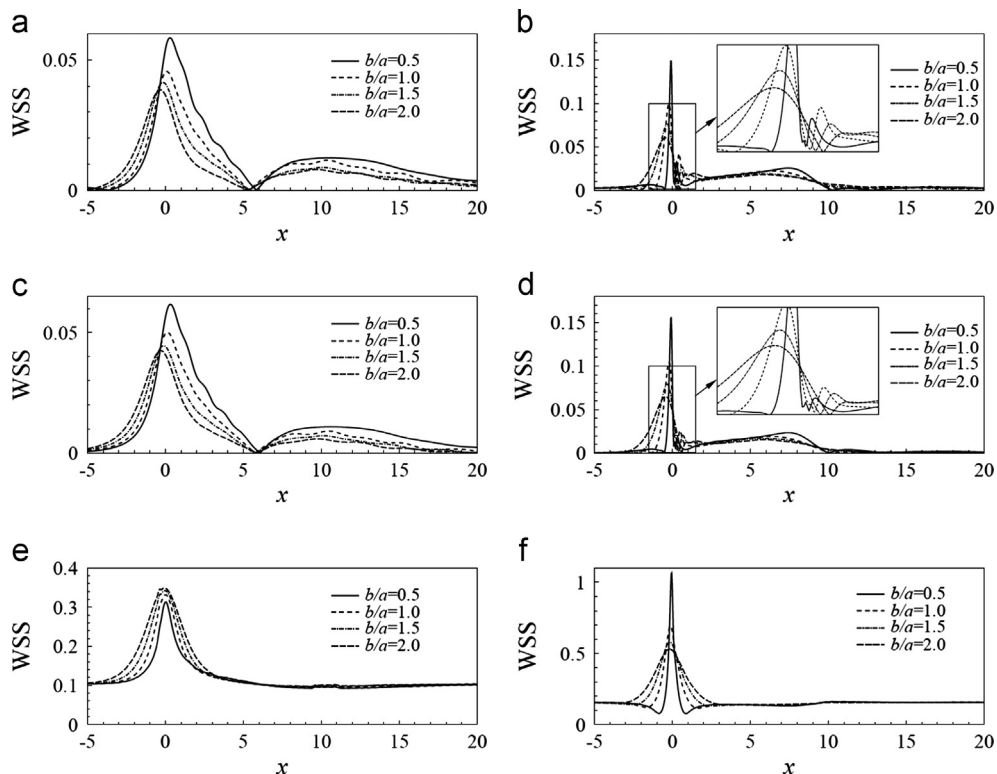
maximum at around P_3, sometime near the end of the diastolic phase. The reason is related to the local evolution of vortices near the boundaries.

Fig. 16 demonstrates some typical flow fields (streamlines, contours of shear rate and vorticity) at three time instants P_1

(top three panels), P_2 (middle three panels), and P_3 (bottom three panels) for $A/a = 1.6$, $b/a = 1.0$. For each instant, the left panel shows the shear rate contours, the right panel shows the vorticity contours, and the bottom panel shows the streamlines. We can see clearly that the flow fields at instant P_1 are similar to the flow
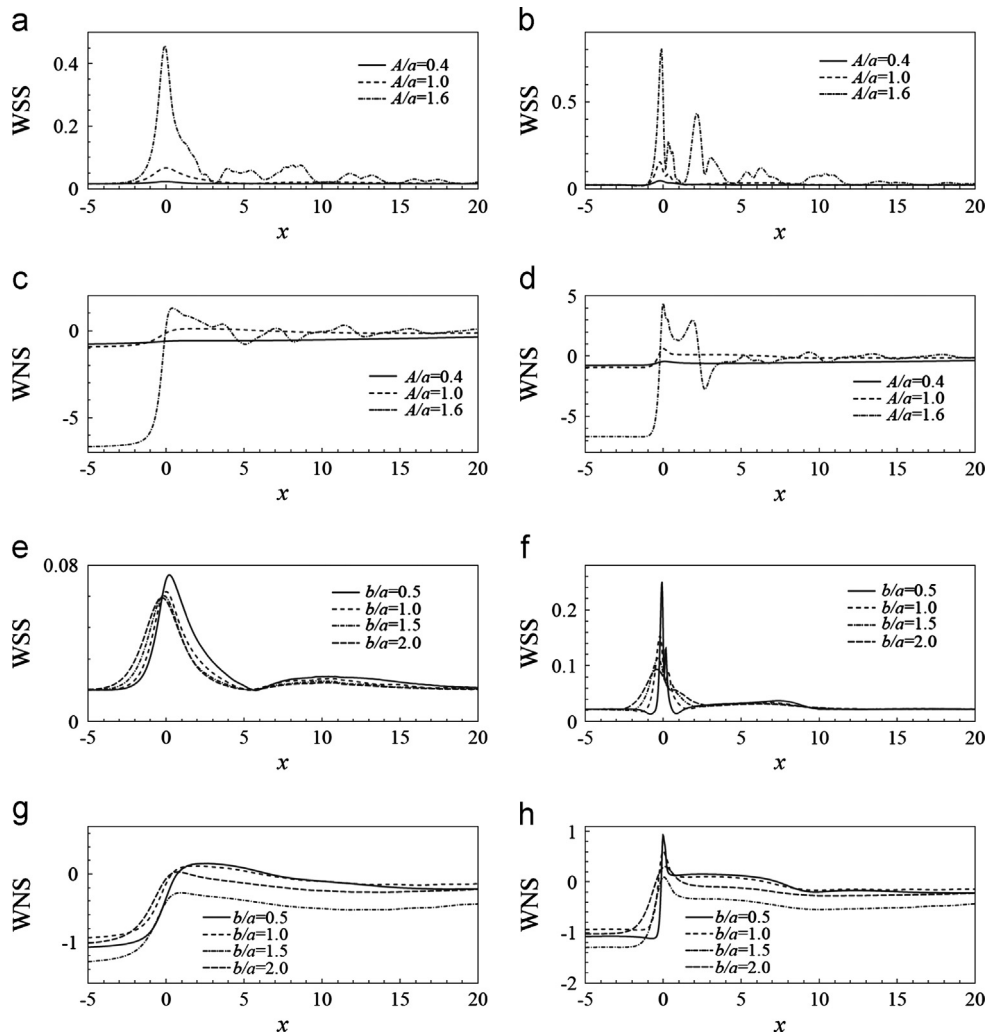
Fig. 15. Time-averaged WSS and WNS of Newtonian pulsatile flow on top (left) and bottom (right) walls for different values of A/a (a–d) and b/a (e–h).

fields at P_2, but both of them are quite different from those at instant P_3. A comparison with Fig. 7 (top right three-panel group) shows that the flow fields of the pulsatile flow are significantly different from the non-pulsatile case. None of the three panels at any instant in Fig. 16 look qualitatively similar to the non-pulsatile steady case in Fig. 7. The difference is caused by the highly unsteady nature of the pulsatile flow.

Although the blood flow is highly unsteady and many variables change with time in a complicated way within a heartbeat (of duration approximately one second), the time-averaged values over an entire heartbeat may be more biologically relevant. For example, remodeling of the arterial wall induced by hemo-dynamics may be more influenced by the time-averaged values of the wall shear stress rather than the instantaneous values of WSS [22]. Therefore we also compute the time-averaged values of WSS and WNS on the walls. Fig. 15 shows the time-averaged values of WSS and WNS on both top and bottom walls. The first two rows show the results with three different values of A/a with $b/a = 1.0$. The first row shows the WSS and the second row shows the WNS. Similarly the last two rows show the results of four different values of b/a with fixed $A/a = 1.0$. In both cases, the left column corresponds to the top wall and the right column corresponds to the bottom wall.

A comparison with Fig. 5 shows that when the value of A/a is small, the time-averaged WSS and WNS are similar to the steady state case; but when A/a is large, obvious differences are observed:

(1) the WSS and WNS on the top wall become very oscillatory after the stenosis; this was not observed in the non-pulsatile case, (2) on the lower wall, the WSS and WNS become highly oscillatory right behind the stenosis; this was also not seen in the non-pulsatile case. However, the oscillations further downstream of the stenosis present in the non-pulsatile case are either absent or are less significant than in the pulsatile case. These observed differ-ences are caused by flow pulsatility and unsteadiness which cannot be eliminated by averaging in time. A comparison with Fig. 6 shows that flow pulsatility has much less effect on WSS and WNS for fixed value of $A/a = 1.0$ with varying values of $b/a = [0.5, 2.0]$. This is probably because the value of $A/a = 1.0$ is not large enough, as discussed above. One discernable difference is that the cusps in WSS and WNS on the bottom wall are smoothed out in the pulsatile case, probably because of the time-averaging.

6.3. Non-Newtonian fluid with pulsatile incoming flow

Figs. 17 and 18 show the WSS versus longitudinal distance x on top and bottom walls for different values of A/a and b/a for the three time instants chosen in the previous section. In both figures, the left column shows the WSS on the top wall and the right column shows the WSS on the bottom wall; the top row corre-sponds to P_1, the middle row corresponds to P_2, and the last row corresponds to P_3.
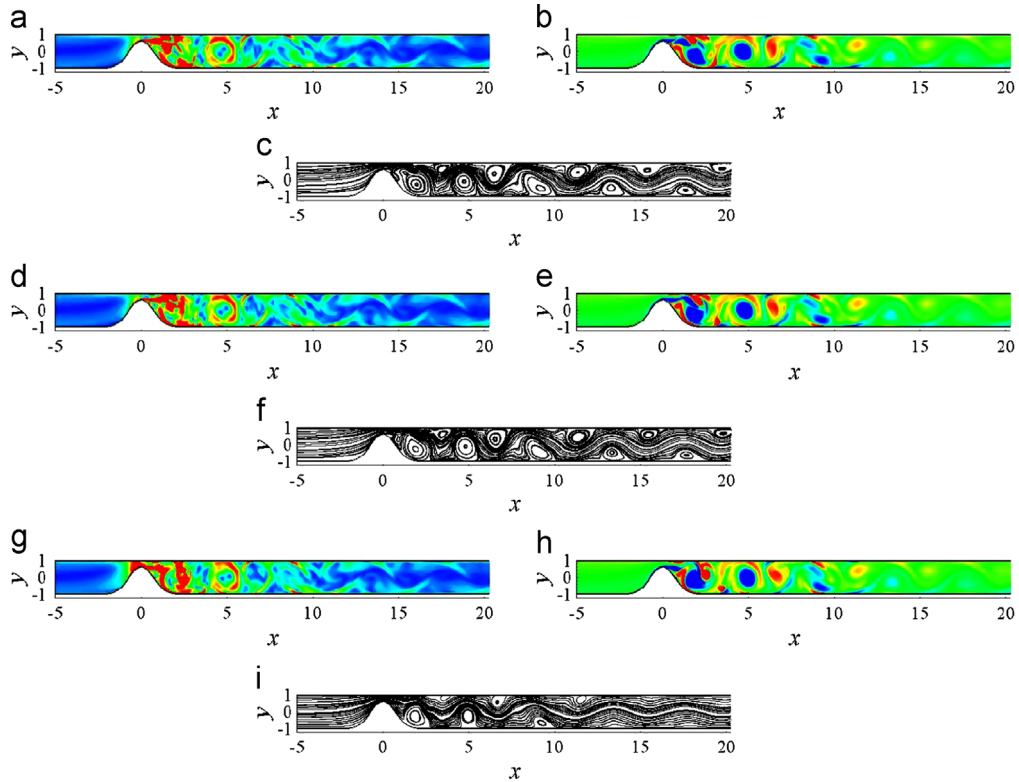
Fig. 16. Contours of SR, vortex field, and streamlines for Newtonian flow. (a) SR at P_1, (b) vorticity at P_1, (c) streamline at P_1, (d) SR at P_2, (e) vorticity at P_2, (f) streamline at P_2, (g) SR at P_3, (h) vorticity at P_3, and (i) streamline at P_3.

Fig. 17. WSS of non-Newtonian pulsatile flow on top (left) and bottom (right) walls at P_1 [(a) and (b)], P_2 [(c) and (d)], and P_3 [(e) and (f)] for different values of A/a.

Compared to the non-pulsatile non-Newtonian cases (Figs. 9 and 10), we see significant oscillations in the WSS on both top and bottom walls in the entire flow domain after the stenosis, rather than just downstream region far away. These substantial variations in WSS are caused by the flow pulsatility and unsteadiness. Also we notice that the WSS distributions are similar at instants P_1 and P_2, but both are very different at instant P_3 when the WSS magnitudes are significantly greater. Again, just as in the
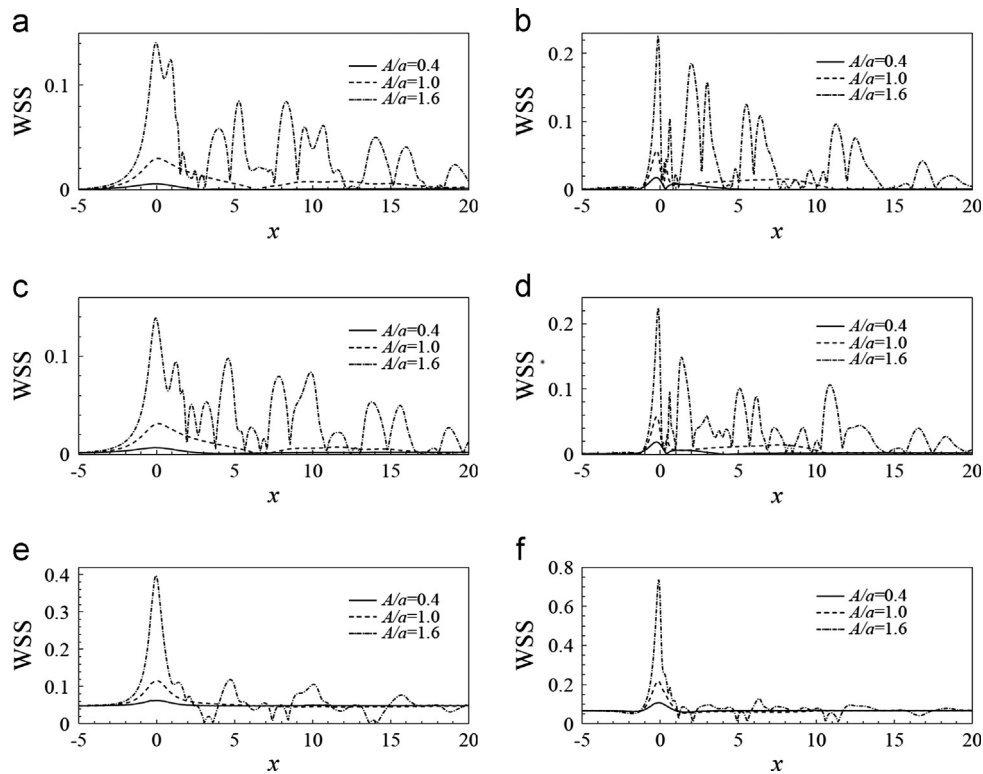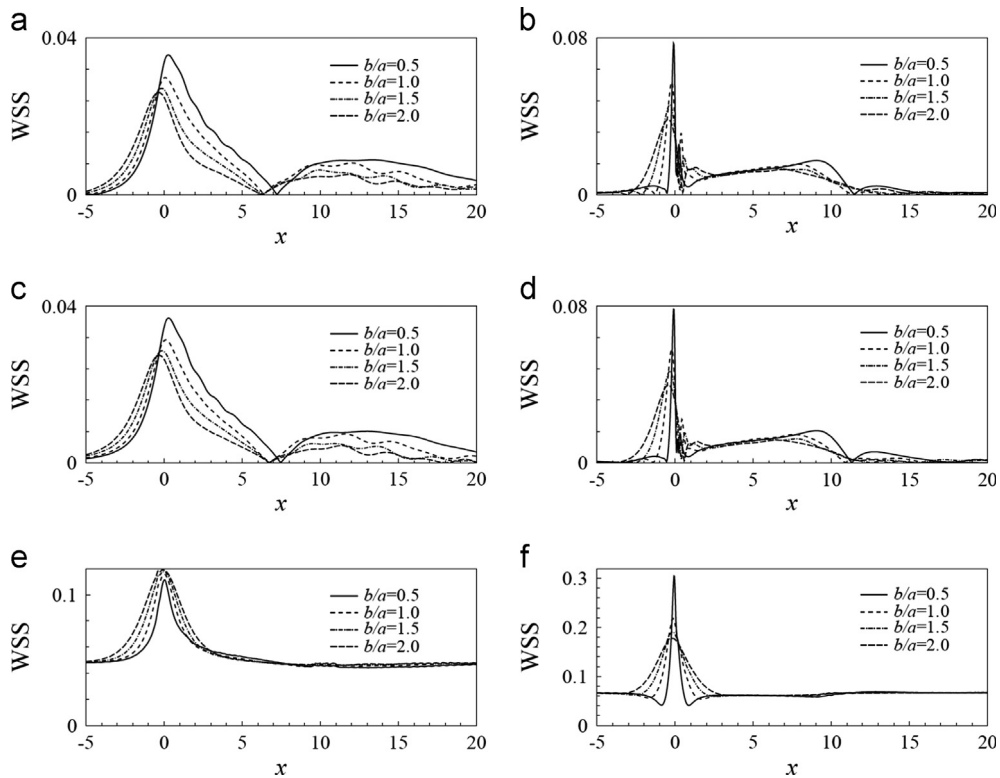
Fig. 18. WSS of non-Newtonian pulsatile flow on top (left) and bottom (right) walls at P_1 [(a) and (b)], P_2 [(c) and (d)], and P_3 [(e) and (f)] for different values of b/a.
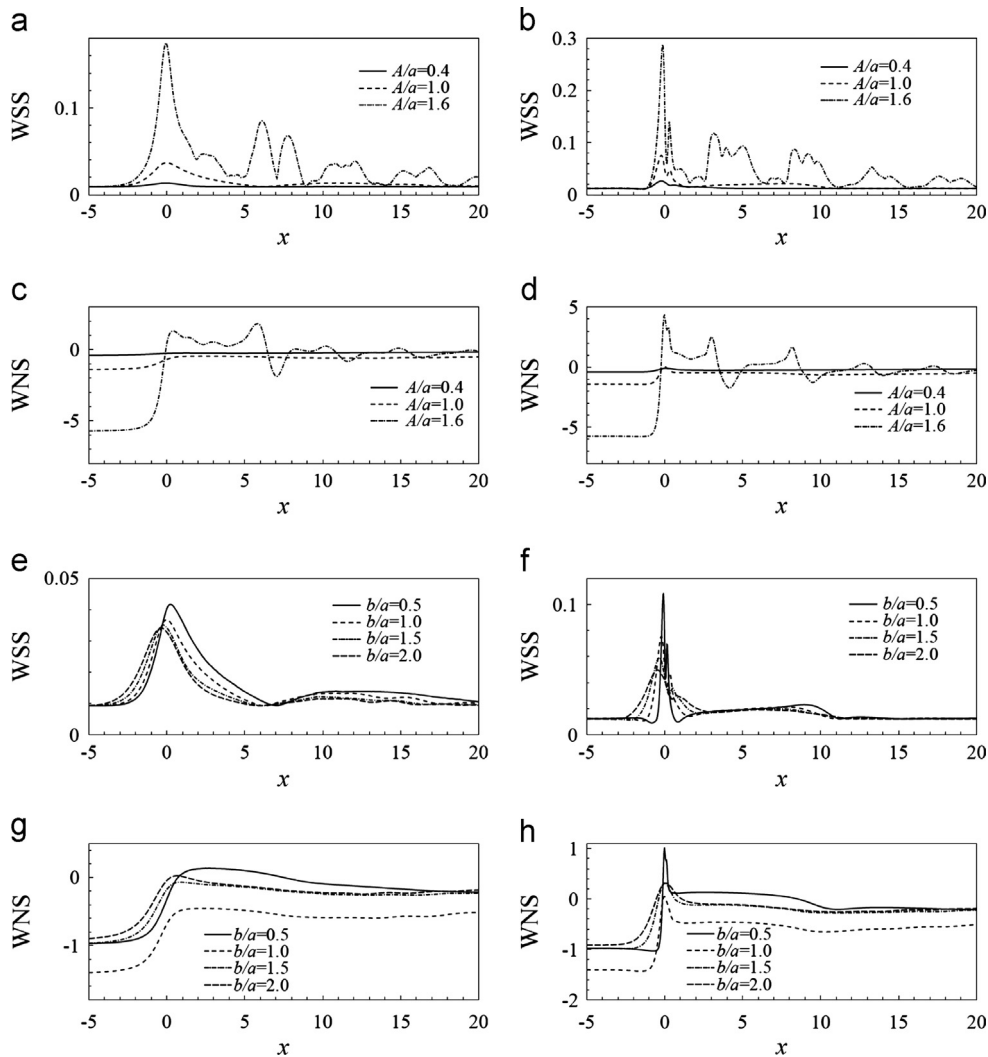
Fig. 19. Time-averaged WSS and WNS of non-Newtonian pulsatile flow on top (left) and bottom (right) walls for different values of A/a (a–d) and b/a (e–h).

pulsatile Newtonian case, the WSS attains its maximum around the instant P_3, sometime near the end of the diastolic phase. Compared to the pulsatile Newtonian case (Figs. 13 and 14), the WSS spatial distribution at the three instants look similar respectively but the WSS magnitudes of the non-Newtonian case are smaller which is because of the shear-thinning property of the non-Newtonian fluid.

Fig. 20 demonstrates some typical flow fields (streamlines, contours of shear rate and vorticity) at three time instants P_1 (top three panels), P_2 (middle three panels), and P_3 (bottom three panels) for $A/a=1.6$, $b/a=1.0$. For each instant, the left panel shows the shear rate contours, the right panel shows the vorticity contours, and the bottom panel shows the streamlines. We can see clearly that the flow fields at instant P_1 are similar to the flow fields at instant P_2, but both of these are quite different from that at instant P_3. Compared to the pulsatile Newtonian case (Fig. 16), we see obvious differences in all of the three fields at each of these three time instants. The pulsatile non-Newtonian case shows substantially higher flow shear rate and richer vorticity dynamics (e.g. more vortices can be seen), in particular in the downstream regions far away from the stenosis. This is caused by the shear thinning of the non-Newtonian fluid. A comparison with the non-pulsatile, non-Newtonian case (Fig. 11, top right three-panel group) again reveals that the pulsatile flow fields are significantly different from the non-pulsatile flow fields. Flow fields at none of the three instants look similar to the steady non-Newtonian case (the averaged flow fields are difficult to obtain). The difference is certainly caused by the highly unsteady nature of the pulsatile flow.

The time-averaged values of WSS and WNS on the two walls are also calculated and plotted. Fig. 19 shows the time-averaged values of WSS and WNS on both top and bottom walls. The first two rows show the results of three different values of A/a with fixed value of $b/a=1.0$. The first row is the WSS and the second row is the WNS. Similarly the last two rows show the results of four different values of b/a with fixed value of $A/a=1.0$. In both cases, the left column corresponds to the top wall and the left column corresponds to the bottom wall. Compared to the pulsatile Newtonian case (Fig. 15), the WSS and WNS of the pulsatile non-Newtonian case are similar on both top and bottom walls when A/a is small, i.e. when the blockage caused by stenosis is not severe. When the value of A/a is sufficiently large, more oscillations in WSS and pressure are seen. In both cases, the magnitude of WSS becomes smaller for the non-Newtonian case for the same reason given in the section on non-Newtonian effect. The magnitude of the pressure remains approximately the same.

A comparison with Figs. 9 and 10 (non-pulsatile non-Newtonian case) shows that when the value of A/a is small, the time-averaged WSS and WNS are similar to the steady state case; but when A/a is large, i.e., for tall plaques, the WSS and WNS on both top and bottom walls become oscillatory right after the stenosis which is not seen in the non-pulsatile case; further downstream of the stenosis, however, the oscillations in WSS and WNS present in the non-pulsatile case become less oscillatory in the pulsatile case. These observed differences may be caused by flow pulsatility and averaging in time.

7. Summary and discussion

We have performed many detailed numerical simulations on an incompressible uniform fluid, both Newtonian and non-Newtonian, past a stenosed 2D artery segment with an idealized atherosclerotic plaque on the lower wall for both steady and pulsatile inlet velocity conditions. Our goal was to make a systematic study of how the hemodynamics is influenced by a variety of factors: the size and geometry of the plaque, Reynolds
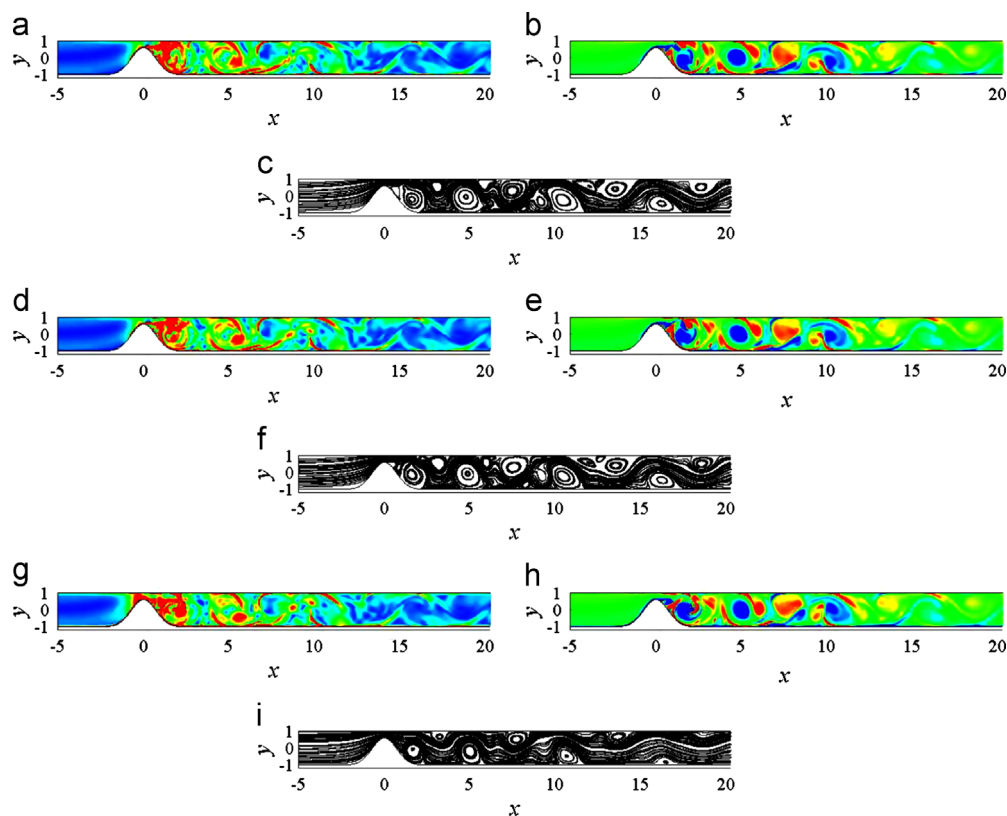

Fig. 20. Contours of SR, vortex field, and streamlines for non-Newtonian flow. (a) SR at P_1, (b) vorticity at P_1, (c) streamline at P_1, (d) SR at P_2, (e) vorticity at P_2, (f) streamline at P_2, (g) SR at P_3, (h) vorticity at P_3, and (i) streamline at P_3.

number, and the shear thinning property of the fluid. We investigated how flow pulsatility affected the magnitude and distribution of wall shear stress (WSS), its gradient (WSSG), wall normal stress (WNS) on the vessel walls, and the flow shear rate (SR) in the entire lumen. Our main conclusions can be summarized as follows: (1) A plaque on one side of an artery alters the flow dynamics in the entire lumen, particularly downstream of the stenosis. The WSS, WSSG, WNS, and SR are all increased on both walls, but the influence on the lower wall is greater. (2) The height of the plaque (A/a) is more influential than the breadth of the plaque (b/a). Stenoses with greater values of A/a and smaller values of b/a significantly change the flow characteristics with respect to a straight channel. They give rise to flow profiles that feature significantly increased WSS, WSSG, and SR; furthermore, WNS is decreased upstream and increased downstream of the plaque. Plaques with smaller A/a and greater b/a impact the flow characteristics much less. (3) Increasing the flow Reynolds number decreases the WSS and increases the WNS and flow SR. (4) The WSS, WSSG and WNS for a non-Newtonian fluid are smaller for a non-Newtonian fluid than for a Newtonian one. The SR for a non-Newtonian fluid is larger. (5) Flow pulsatility generates substantial oscillations in WSS, WNS, WSSG, and SR.

Our results may explain why straight arteries tend to be more resistant to atherosclerosis than curved or bifurcated ones. Since stenoses in straight arteries generally *increase* the wall stress, under the conditions of the low endothelial shear stress hypothesis, these parts of the blood vessel would *not* be rendered susceptible to plaque formation through the normal methods outlined by the hypothesis. However, we can only speculate on whether plaques are more or less likely to form in regions of high fluid shear stress. Some experiments, in fact, suggest that high WSS may increase endothelial permeability [42]. Furthermore, increased WNS/pressure may increase the flux of macromolecules such as LDL through the endothelium and vessel walls, and may in theory promote plaque formation. Hence the interpretation of force distributions along the vessel wall remains enigmatic and the calculation of fluid stress profiles induced by lesions – together with the implications for biochemistry and transport within the vessel walls – remain important areas of research in computational fluid dynamics.

The actual physiological blood flow in human vessels is three dimensional and quite challenging to model and simulate because of the complicated geometry of blood vessels. A lack of realistic boundary conditions for the fluid velocity on the endothelial surface layer presents additional difficulties. Although 3D computations of blood flow exist in the literature, to the best of our knowledge, there are no systematic studies that characterize the forces on a plaque in as much detail as we have done in this paper. As one may see from Section 3, 2D simulation can capture some features of 3D flows and may provide some insights into the physics of such flows. With this said, we foresee that 3D simulations will be necessary for improved understanding of the WSS, WSSG, WNS, and flow SR.

Blood flow in normal healthy human vessels is usually laminar due to the relatively low Reynolds numbers, the non-Newtonian nature of the blood and the pulsatility of the flow [26,9,11]. Although blood is shear thinning, non-Newtonian flow is qualitatively similar to Newtonian flow at lower Reynolds numbers [12–14], and flow pulsatility tends to suppress the growth of turbulence [45]. However, blood flow past severely stenosed arteries could be turbulent [20,3]. In our current work the modeling and simulation are performed in two dimensions, and turbulence in 2D and 3D is qualitatively different [33]; therefore we do not consider possible turbulence effects when the vessel is severely stenosed. Presumably the turbulent blood flow in three dimensions may alter the flow and force fields to some degree

depending on the intensity of the turbulence, particularly near the stenotic region. The WSS, WSSG, WNS, SR may become stochastic and their extreme values may be biologically interesting. Modeling and simulating blood flow past a stenosis in three dimensions, while incorporating possible turbulent effects, is a natural yet challenging extension of our current work, and one which we plan to pursue in the future.

Conflict of interest statement

None declared.

Acknowledgments

References

[1] A.D. August, B. Ariff, S.A.G. Thom SMcG, X.Y. Xu, A.D. Hughes, Analysis of complex flow and relationship between blood pressure, wall shear stress, and intima-media thickness in the human carotid artery, Am. J. Physiol. Heart Circ. Physiol. 293 (2007) 1031–1037.

[2] J. Bale-Glickman, K. Selby, D. Saloner, O. Savas, Experimental flow studies in exact-replica phantoms of atherosclerotic carotid bifurcations under steady input conditions, J. Biomech. Eng. 125 (2003) 38–48.

[3] T.J. Barber, A. Simmons, Large eddy simulation of a stenosed artery using a femoral artery pulsatile flow profile, Artif. Organs 35 (2011) E155–E160.

[4] R.L. Bratzler, C.K. Colton, K.A. Smith, Theoretical models for transport of low-density lipoproteins in the arterial wall, Adv. Exp. Med. Biol. 82 (1977) 943–951.

[5] C.G. Caro, J.M. Fitz-Gerald, R.C. Schroter, Arterial wall shear and distribution of early atheroma in man, Nature (1969) 1159–1161.

[6] C.G. Caro, J.M. Fitz-Gerald, R.C. Schroter, Atheroma and arterial wall shear. observation, correlation and proposal of a shear dependent mass transfer mechanism for atherogenesis, Proc. R. Soc. London B 177 (1971) 109–133.

[7] Y.S. Chatzizisis, A.U. Coskun, M. Jonas, E.R. Edelman, C.L. Feldman, P.H. Stone, Role of endothelial shear stress in the natural history of coronary atherosclerosis and vascular remodeling: molecular cellular, and vascular, behavior, J. Am. Coll. Cardiol. 49 (2007) 2379–2393.

[8] H.Y. Chen, J. Hermiller, A.K. Sinha, M. Sturek, L. Zhu, G.S. Kassab, Effects of intravascular stent sizing on endothelial and vessel wall stress: potential mechanisms of in-stent restenosis, J. Appl. Physiol. 106 (2009) 1686–1691.

[9] H.Y. Chen, L. Zhu, Y. Huo, Y. Liu, G.S. Kassab, Fluid–structure interaction (fsi) modeling in the cardiovascular system, in: J.M. Guccione, G.S. Kassab, M.B. Ratcliffe (Eds.), Computational Cardiovascular Mechanics, Springer, 2010, pp. 141–157.

[10] H.Y. Chen, A.K. Sinha, J.S. Choy, H. Zheng, M. Sturek, B. Bigelow, D. Bhatt, G.S. Kassab, Mis-sizing of stent promotes intimal hyperplasia: impact of endothelial shear and intramural stress, Am. J. Physiol. Heart Circ. Physiol. 301 (2011) H2254–H2263.

[11] H.Y. Chen, I.D. Moussa, C. Davidson, G.S. Kassab, Impact of main branch stenting on endothelial shear stress: role of side branch diameter, angle and lesion, J. R. Soc. Interface 9 (2012) 1187–1193.

[12] J. Chen, X. Lu, Numerical investigation of the non-Newtonian blood flow in a bifurcation model with a non-planar branch, J. Biomech. 37 (2004) 1899–1911.

[13] J. Chen, X.Y. Lu, Numerical investigation of the non-Newtonian pulsatile blood flow in a bifurcation model with a non-planar branch, J. Biomech. 39 (2006) 818–832.

[14] J. Chen, X. Lu, W. Wang, Non-Newtonian effects of blood flow on hemodynamics in distal vascular graft anastomoses, J. Biomech. 39 (2006) 1983–1995.

[15] S. Chien, Molecular and mechanical bases of focal lipid accumulation in arterial wall, Prog. Biophys. Mol. Biol. 83 (2003) 131–151.

[16] C.A. Cobbold, J.A. Sherratt, S.R.J. Maxwell, Lipoprotein oxidation and its significance for atherosclerosis: a mathematical approach, Bull. Math. Biol. 64 (2002) 65–95.

[17] P.F. Fischer, F. Loth, S.E. Lee, S.W. Lee, D. Smith, H. Bassiouny, Simulation of high Reynolds number vascular flows, Comput. Methods Appl. Mech. Eng. 196 (2007) 3049–3060.

[18] F.J.H. Gijsen, F.N. van de Vosse, J.D. Janssen, The influence of the non-Newtonian properties of blood on the flow in large arteries: steady flow in a carotid bifurcation model, J. Biomech. 32 (1999) 601–608.

[19] F.J.H. Gijsen, F.N. van de Vosse, J.D. Janssen, The influence of the non-Newtonian properties of blood on the flow in large arteries: unsteady flow in a 90° curved tube, J. Biomech. 32 (1999) 705–713.

[20] L. Grinberg, A. Yakhot, G.E. Karniadakis, Analyzing transient turbulence in a stenosed carotid artery by proper orthogonal decomposition, Ann. Biomed. Eng. 37 (2009) 2200–2217.

[21] H.A. Himburg, D.M. Grzybowski, A.L. Hazel, J.A. LaMack, X.M. Li, M.H. Friedman, Spatial comparison between wall shear stress measures and porcine arterial endothelial permeability, Am. J. Physiol. Heart Circ. Physiol. 286 (2004) H1916–H1922.

[22] T.K. Hsiai, S.K. Cho, S. Reddy, S. Hama, M. Navab, L.L. Demer, H.M. Honda, C.M. Ho, Pulsatile flow regulates monocyte adhesion to oxidized lipid-induced endothelial cells, Arterioscler. Thromb. Vasc. Biol. 21 (2001) 1770–1776.

[23] F.L. Keegan, Experimental Investigation into Non-Newtonian Fluid Flow Through Gradual Contraction Geometries, Ph.D. Thesis, University of Liverpool, 2009.

[24] U. Kohler, I. Marshall, M.B. Robertson, Q. Long, X.Y. Xu, MRI measurement of wall shear stress vectors in bifurcation models and comparison with CFD predictions, J. Magn. Reson. Imaging 14 (2001) 563–573.

[25] A. Kovacs, M. Kawahara, A finite element scheme based on the velocity correction method for the solution of the time-dependent incompressible Navier–Stokes equations, Int. J. Numer. Methods Fluids 13 (1991) 403–423.

[26] D.N. Ku, Blood flow in arteries, Annu. Rev. Fluid Mech. 29 (1997) 399–434.

[27] J.R. Levick, An Introduction to Cardiovascular Physiology, 5th ed., Hodder Arnold, London, 2010.

[28] Q. Liao, G.J. Dong, X.Y. Lu, Vortex formation and force characteristics of a foil in the wake of a circular cylinder, J. Fluids Struct. 19 (2004) 491–510.

[29] P. Libby, P. Ridker, G. Hansson, Progress and challengers in translating the biology of atherosclerosis, Nature 473 (2011) 317–325.

[30] X.Y. Lu, Q. Liao, Dynamic responses of a two-dimensional flapping foil motion, Phys. Fluids 18 (2006) 098104.

[31] U. Olgac, V. Kurtcuoglu, D. Poulikakos, Computational modeling of coupled blood-wall mass transport of LDL: effects of local wall shear stress, Am. J. Physiol. Heart Circ. Physiol. 294 (2008) H909–H919.

[32] T.L. Poepping, R.N. Rankin, D.W. Holdsworth, Flow patterns in carotid bifurcation models using pulsed Doppler ultrasound: effect of concentric vs. eccentric stenosis on turbulence and recirculation, Ultrasound Med. Biol. 36 (2010) 1125–1134.

[33] S. Pope, Turbulent Flows, Cambridge University Press, 2000.

[34] S.B.H. Shah, X.Y. Lu, Numerical simulation of an oscillating flow past a circular cylinder in the vicinity of a plane wall, J. Hydrodyn. 20 (2008) 547–552.

[35] D.A. Steinman, T.L. Poepping, M. Tambasco, R.N. Rankin, D.W. Holdsworth, Flow patterns at the stenosed carotid bifurcation: effect of concentric versus eccentric stenosis, Ann. Biomed. Eng. 28 (2000) 415–423.

[36] P. Stroev, P. Hoskins, W. Easson, Distribution of wall shear rate throughout the arterial tree: a case study, Atherosclerosis 191 (2007) 276–280.

[37] J.S. Stroud, S.A. Berger, D. Saloner, Numerical analysis of flow through a severely stenotic carotid artery bifurcation, J. Biomech. Eng. 124 (2002) 9–20.

[38] F.P.P. Tan, G. Soloperto, S. Bashford, et al., Analysis of flow disturbance in a stenosed carotid artery bifurcation using two-equation transitional and turbulence models, J. Biomech. Eng. 130 (2008) 061008.

[39] Y. Tardy, N. Resnick, T. Nagek, M. Gimbrone Jr., C. Dewey Jr., Shear stress gradients remodel endothelial monolayers in vitro via a cell proliferation-migration-loss cycle, Arterioscler. Thromb. Vasc. Biol. 17 (1997) 3102–3106.

[40] Z. Teng, G. Canton, C. Yuan, M. Ferguson, C. Yang, X. Huang, J. Zheng, P. Woodard, D. Tang, 3D critical plaque wall stress is a better predictor of carotid plaque rupture sites than flow shear stress: an in vivo MRI-based 3D FSI study, J. Biomech. Eng. T. ASME 132 (2010) 031007.

[41] M.J. Thubrikar, Vascular Mechanics and Pathology, Springer, New York, 2007.

[42] C.M. Warboys, R. Eric Berson, G.E. Mann, J.D. Pearson, P.D. Weinberg, Acute and chronic exposure to shear stress have opposite effects on endothelial permeability to macromolecules, Am. J. Physiol. Heart Circ. Physiol. 298 (2010) H1850–H1856.

[43] E.Y. Wong, H.N. Nikolov, M.L. Thorne, T.L. Poepping, R.N. Rankin, D.W. Holdsworth, Clinical Doppler ultrasound for the assessment of plaque ulceration in the stenosed carotid bifurcation by detection of distal turbulence intensity: a matched model study, Eur. Radiol. 19 (2009) 2739–2749.

[44] J.Z. Wu, H.Y. Ma, M.D. Zhou, Vorticity and Vortex Dynamics, Springer-Verlag, Berlin, 2006.

[45] E.L. Yellin, Laminar–turbulent transition process in pulsatile flow, Circ. Res. 19 (1966) 791–804.